



HAL
open science

Functional carbon quantum dots as medical countermeasures to human coronavirus (HCoV)

Aleksandra Loczechin, Karin Séron, Alexandre Barras, Emerson Giovanelli, Sandrine Belouzard, Yen-Ting Chen, Nils Metzler-Nolte, Rabah Boukherroub, Jean Dubuisson, Sabine Szunerits

► To cite this version:

Aleksandra Loczechin, Karin Séron, Alexandre Barras, Emerson Giovanelli, Sandrine Belouzard, et al.. Functional carbon quantum dots as medical countermeasures to human coronavirus (HCoV). ACS Applied Materials & Interfaces, 2019, 11 (46), pp.42964-42974. 10.1021/acsami.9b15032 . hal-02328361

HAL Id: hal-02328361

<https://hal.science/hal-02328361v1>

Submitted on 6 Nov 2020

HAL is a multi-disciplinary open access archive for the deposit and dissemination of scientific research documents, whether they are published or not. The documents may come from teaching and research institutions in France or abroad, or from public or private research centers.

L'archive ouverte pluridisciplinaire **HAL**, est destinée au dépôt et à la diffusion de documents scientifiques de niveau recherche, publiés ou non, émanant des établissements d'enseignement et de recherche français ou étrangers, des laboratoires publics ou privés.

Functional Carbon Quantum Dots as Medical Countermeasures to Human Coronavirus

Aleksandra Łoczechin,^{†,‡} Karin Séron,[§] Alexandre Barras,^{†,‡} Emerson Giovanelli,^{†,‡} Sandrine Belouard,[§] Yen-Ting Chen,^{||} Nils Metzler-Nolte,^{‡,||} Rabah Boukherroub,^{†,||} Jean Dubuisson,^{*,§} and Sabine Szunerits^{*,†,||}

[†]University of Lille, CNRS, Centrale Lille, ISEN, Universit of Valenciennes, UMR 8520 - IEMN, Lille F-59000, France

[‡]Inorganic Chemistry I, Bioinorganic Chemistry, Faculty of Chemistry and Biochemistry, Ruhr University Bochum,

Universitätstrasse 150, Bochum 44801, Germany

[§]University of Lille, CNRS, INSERM, CHU Lille, Institut Pasteur de Lille, CIIL - Center for Infection and Immunity of Lille,

U1019 - UMR 8204, Lille F-59000, France

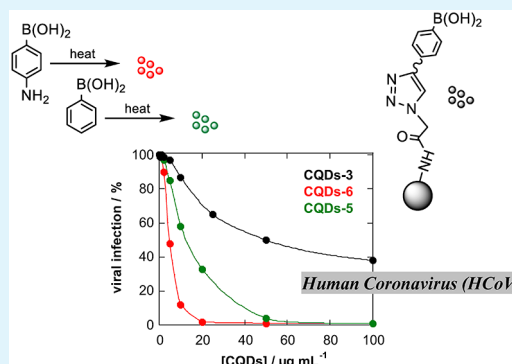
^{||}Center of Molecular Spectroscopy and Simulation of Solvent-driven Processes (ZEMOS), Ruhr-University Bochum,

Bochum 44801, Germany

S Supporting Information

ABSTRACT: Therapeutic options for the highly pathogenic human coronavirus (HCoV) infections are urgently needed. Anticoronavirus therapy is however challenging, as coronaviruses are biologically diverse and rapidly mutating. In this work, the antiviral activity of seven different carbon quantum dots (CQDs) for the treatment of human coronavirus HCoV-229E infections was investigated. The first generation of antiviral CQDs was derived by hydrothermal carbonization from ethylenediamine/citric acid as carbon precursors and postmodified with boronic acid ligands. These nanostructures showed a concentration-dependent virus inactivation with an estimated EC_{50} of $52 \pm 8 \mu\text{g mL}^{-1}$. CQDs derived from 4-aminophenylboronic acid without any further modification resulted in the second-generation of anti-HCoV nanomaterials with an EC_{50} lowered to $5.2 \pm 0.7 \mu\text{g mL}^{-1}$. The underlying mechanism of action of these CQDs was revealed to be inhibition of HCoV-229E entry that could be due to interaction of the functional groups of the CQDs with HCoV-229E entry receptors; surprisingly, an equally large inhibition activity was observed at the viral replication step.

KEYWORDS: human coronavirus (HCoV), carbon quantum dots (CQDs), antiviral therapy, boronic acid, multivalent interactions



1. INTRODUCTION

The eradication of viral infections is an ongoing challenge in the medical field, not only due to the problem of spreading but also to the virus' ability to escape therapy by genetic mutations. The lack of targeted antiviral therapeutics as well as the constant emergence of new viruses make the search for antiviral agents a challenging and extremely needed research task.¹ As part of a global strategy to prevent epidemics, some severe emerging pathogens with great epidemic potential have been identified by the World Health Organization (WHO),² including, next to Ebola virus disease, the highly pathogenic human coronavirus (HCoV) infections. While circulating HCoVs (HCoV-229E, HCoV-OC43, HCoV-NL63, and HKU1) cause relatively mild common cold-like respiratory tract infections, severe acute respiratory syndrome coronavirus (SARS-CoV) and Middle-East respiratory syndrome coronavirus (MERS-CoV) lead to pneumonia requiring hospitalization and intensive care.³ A total of 2266 laboratory-confirmed cases of MERS-CoV, including 804 associated deaths, have been declared to the WHO until now, with a

high case-fatality rate (35%).⁴ As the virus is circulating in animals and humans, it may undergo further adaptation and cause a pandemic. Therefore, therapeutic options are urgently needed.

The current treatments for MERS-CoV are extrapolated from SARS-CoV and H1N1 influenza outbreaks.^{5–7} These include different combinations of small molecules with broad antiviral activity (e.g., ribavirin, corticosteroids, and interferons (IFN)), and monoclonal and polyclonal antibody therapies.^{7,8} The membrane-anchored glycoprotein S has lately been found to be essential for the interaction between the MERS-CoV and the host cell,^{8,9} and the development of MERS-CoV entry/fusion inhibitors targeting the S1 subunit is nowadays considered as a viable antiviral strategy.

Recently, nanoscale materials have emerged as promising and efficient platforms to modulate the viral infection cycle.¹⁰ Given

Received: August 22, 2019

Accepted: October 21, 2019

Published: October 21, 2019

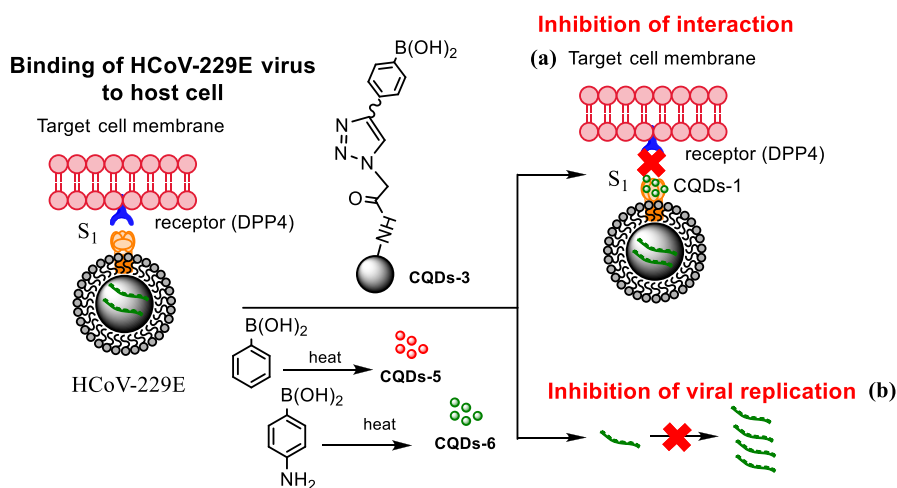


Figure 1. Influence of CQDs, prepared by hydrothermal carbonization, on binding of HCoV-229E virus to cells: (a) inhibition of protein S receptor interaction, and (b) inhibition of viral RNA genome replication.

64 that attachment of viruses into host cells is favored by multi-
65 valent interactions, the multivalent character of nanostructures
66 with their high surface to volume ratio, allowing the attachment
67 of several ligands, makes them well adapted to interfere with viral
68 attachment and blocking viral entry into cells.

69 In this work, we investigate the potential of functional carbon
70 quantum dots (CQDs) as inhibitors of host cells infection by
71 HCoV-229E coronavirus (Figure 1). CQDs with an average
72 diameter below 10 nm and excellent water solubility are highly
73 attractive for nanomedical applications due to a lack of visible
74 signs of toxicity in animals.¹¹ They can be synthesized quickly via
75 several different inexpensive and simple methods, and their
76 excellent optical properties offer in vivo tracking possibilities.
77 It was recently demonstrated that CQDs are suitable scaffolds to
78 interfere with the entry of viruses into cells.^{12–14} Boronic acid-
79 modified CQDs were able to inhibit, for example, HIV-1 entry
80 by suppressing syncytium formation.¹³ Some of us have shown
81 lately the potential of CQDs-functionalized with boronic acid
82 and amine moieties to interfere with the entry of herpes simplex
83 virus type 1.¹² Han and co-workers reported lately the potential
84 of CQDs as viral inhibitors by activation of type I interferon
85 responses.¹⁴

86 This unique study reveals that boronic acid functions can be
87 responsible for the anti-HCoV activity. CQDs derived from
88 citric acid/ethylenediamine and further conjugated by “click”
89 chemistry with boronic acid functions display an effective 50%
90 inhibition concentration $EC_{50} = 52 \pm 8 \mu\text{g mL}^{-1}$. Likewise, CQDs
91 derived from 4-aminophenylboronic acid and phenylboronic acid
92 without any further modification exhibit antiviral behavior with a
93 decreased effective EC_{50} down to $5.2 \pm 0.7 \mu\text{g mL}^{-1}$. The
94 underlying mechanism of action of these CQDs was revealed to
95 be the CQDs interaction with the HCoV-229E S protein.
96 Surprisingly, an equally large inhibition activity was observed at
97 the viral replication step.

2. RESULTS AND DISCUSSION

98 **2.1. First-Generation of CQDs Inhibitors of Host Cell**
99 **Infections by HCoV-229E Coronavirus: Boronic Acid-**
100 **Modified CQDs.** **2.1.1. Formation and Characterization.**
101 **Carbon Quantum Dots Formed from Ethylenediamine/Citric**
102 **Acid.** Boronic acid derivatives have been proposed as low-
103 toxicity agents for inhibiting the entry of various viruses.^{15,16}
104 To test if such concepts can be extrapolated to human

coronavirus HCoV-229E infections, boronic acid functional 105
groups were chemically integrated onto CQDs-1 formed 106
through hydrothermal carbonization of ethylenediamine/citric 107
acid (Figure 2A). The approach consists of sealing the organic 108
precursors within a Teflon-lined autoclave chamber and 109
performing the formation of CQDs at elevated temperature 110
under reduced pressure for 5 h. The pH value of the resulting 111
CQDs suspensions was found to be 7.2 ± 0.2 ($n = 5$). To remove 112
larger precipitates, the as-obtained CQDs suspension was first 113
centrifuged and then dialyzed against water for 24 h with a final 114
yield of CQDs of 40%. CQDs-1 exhibit a spherical shape with an 115
average diameter of 4.5 ± 0.2 nm (Figure 2B). XPS analysis 116
(Table 1) indicates the presence of C, O, and N. The C_{1s} high- 117
resolution XPS spectrum of CQDs-1 depicts three different 118
carbon features: the graphitic C=C at 283.4 eV, 284.9 eV (C–H), 119
and 286.4 eV (C–O, C–N) (Figure 2C). Analysis of the N_{1s} 120
high-resolution XPS shows the presence surface NH_2 groups 121
(399.9 eV) (Figure 2D). The Raman spectrum of the CQD-1 122
(Figure 2E) displays the characteristic G band at 1570 cm^{-1} 123
related to in-plane vibration of sp^2 carbon, and the D band at 124
 1350 cm^{-1} attributed to disorder and defects. The ratio of the 125
intensity of these bands (I_D/I_G), used to express the extent of 126
 sp^2/sp^3 hybridization of carbon atoms,¹⁷ is found to be $0.93 \pm$ 127
 0.15 for all particles.¹⁸ XRD patterns indicate their crystalline 128
nature (see Figure S1A) with a broad diffraction peak centered 129
at 25.5° corresponding to an interlayer spacing of 0.35 nm. This 130
is larger than the spacing between (100) planes in bulk graphite 131
(0.23 nm) due to the incorporation of functional groups along 132
the edges of the CQDs.¹⁹ The UV/vis of CQDs-1 (see Figure S1B) 133
reveals an absorption maximum at ~ 242 nm attributed to $\pi-\pi^*$ 134
transition of C=C and a band at 344 nm due to $n-\pi^*$ transition 135
of C=O and C=N bonds.^{20,21} The fluorescence quantum yield 136
(QY) is 0.33 as compared to that of quinine sulfate used as 137
reference (QY, 0.54 in 0.12 M H_2SO_4) (see Figure S1C). 138
A wavelength-dependent fluorescence emission is observed (see 139
Figure S1D) where upon increasing the excitation wavelength, 140
the emission gradually shifts to the red region with an increase in 141
fluorescence intensity. The phenomenon of excitation-depend- 142
ent emission is typical for such nanostructures.^{5–7} The zeta 143
potential and hydrodynamic size of the CQDs-1 are summarized 144
in Table 1. 145

Functionalization of CQDs-1. The formation of CQDs-3 146
is based on a two-step chemical process. In a first step, 147

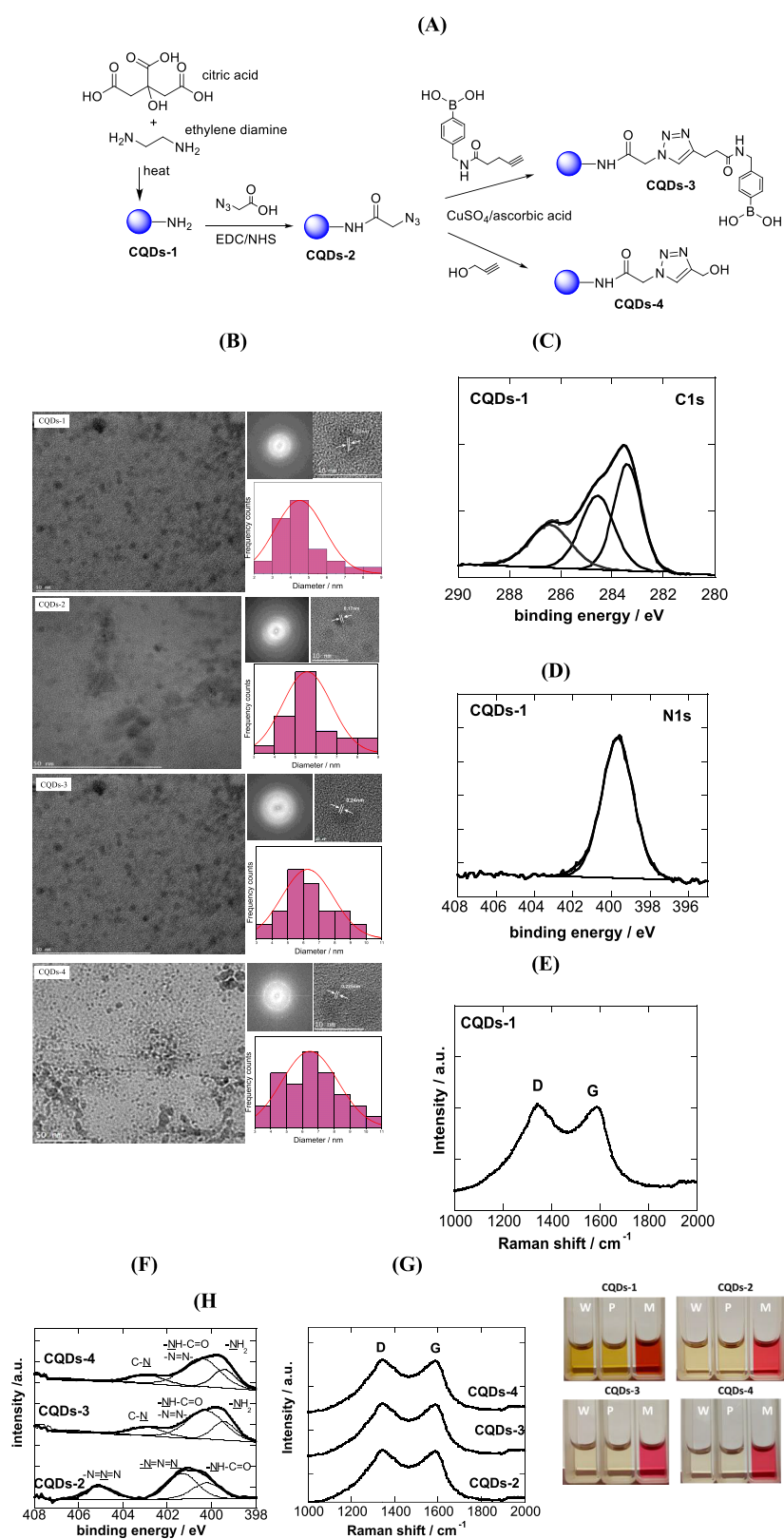


Figure 2. (A) Schematic representation of the synthesis of CQDs-1–4; (B) TEM, magnified TEM, HR-TEM images, and size distribution histograms of CQDs-1–4; (C) C_{1s} high-resolution XPS spectrum of CQDs-1; (D) N_{1s} high-resolution XPS spectrum of CQDs-1; (E) Raman spectrum of CQDs-1; (F) N_{1s} high-resolution XPS spectrum of CQDs-2–4; (G) Raman spectrum of CQDs-2–4; and (H) photographs of CQDs-1–4 suspensions (1 mg mL^{-1}) after 1 month in water (W), PBS (0.01 M, P), and Dulbecco's Modified Eagle's medium (M).

148 azido-functionalized CQDs-2 are prepared by coupling 2-azido
149 acetic acid moieties to CQDs-1. The N_{1s} signal of CQDs-2
150 shows signals at 405.2 ($-\text{N}=\text{N}^+=\text{N}^-$) and 401.6 eV

($\text{N}=\text{N}^+=\text{N}^-$) in a 1:2 ratio, as theoretically expected 151
(Figure 2F). The azide functions in CQDs-2 quantitatively 152
react with alkyne functions as indicated by the absence of the 153

Table 1. Physico-chemical Characteristics of the CQDs

CQDs	ζ (mV) ^a	size (nm)	hydrodynamic size (nm) ^b	PDI	C _{1s} ^c (at. %)	O _{1s} (at. %)	N _{1s} (at. %)	B _{1s} (at. %)
CQDs-1	-9.9 ± 3.4	4.5 ± 0.2	11 ± 0.1	0.22 ± 0.11	72.6	12.5	14.9	
CQDs-2	-7.9 ± 2.7	5.5 ± 0.3	12 ± 0.1	0.23 ± 0.11	68.8	13.9	17.3	
CQDs-3	-15.9 ± 4.3	6.3 ± 0.4	12 ± 0.25	0.15 ± 0.10	67.9	7.3	20.3	4.5
CQDs-4	-15.9 ± 1.3	6.5 ± 0.4	11 ± 0.19	0.13 ± 0.10	68.5	13.6	17.9	

^a ζ , zeta potential; PDI, polydispersity index. ^bThe hydrodynamic size was recorded at 37 °C. ^cXPS was used to determine the atomic percentage of the elements, respectively.

azide band at 405.2 eV in the relevant spectra of CQDs-3 and CQDs-4 (Figure 2F). The band at 399.2 eV (–NH₂) is most likely resulting from partial hydrolysis of surface linked 2-azido acetic ester function. CQDs-4 were synthesized as a control check whether the triazole function acts as a passive linker or not.^{22,23} The morphologies of CQDs-3 and CQDs-4 are comparable to that of CQDs-1 with an average diameter of 6.25 ± 0.17 nm (Figure 2B) and diffraction peak centered at 25.3° for CQDs-3 (see Figure S1A) and an average diameter of 6.50 ± 0.40 nm (Figure 2B) and diffraction peak centered at 25.4° for CQDs-4. The Raman spectra of the CQDs-2–4 (Figure 2G) remain indifferent to that of CQDs-1 displaying the characteristic G and D bands with I_D/I_G = 0.93 ± 0.15 for all particles.¹⁸ The colloidal stability of CQDs-1–4 in water, phosphate buffer (PBS, 10 mM), and Dulbecco's Modified Eagle's medium (M) was, in addition, examined. All of the particles had good long-term colloidal stability as seen from the photographs in Figure 2H.

2.1.2. Cytotoxicity Assay. The cell toxicity of CQDs-1, CQDs-3, and CQDs-4 was established on Huh-7 cell lines after 8 h (time points corresponding to HCoV-229E infections) and 24 h incubation. The CQDs toxicity was evaluated using cell viability assessment by the resazurin assay, based on the conversion of nonfluorescent dye to a fluorescent molecule by mitochondrial and cytoplasmic enzymes. All CQDs are nontoxic to Huh-7 cells even at the highest concentration (100 μg mL⁻¹) investigated when incubated for 8 and 24 h (Figure 3A). Neither the presence of boronic acid nor triazole units had a negative effect on cell toxicity.

The uptake mechanism proved to be the same for all of the nanostructures. Taking the example of CQDs-3 (which later proves to have antiviral activity), Huh-7 cells were fixed after 1 h incubation at 4 and 37 °C, and then nuclei were stained with Hoechst 33342, a fluorescent dye for labeling DNA in fluorescence microscopy (Figure 3B). The green fluorescence, which is attributed to the CQDs-3, is homogeneously distributed in the cytoplasm after 1 h when incubated at 37 °C, which confirms the internalization of CQDs-3 inside the cells. The reduction of green fluorescence, observed in the cytoplasm after 1 h incubation at 4 °C, suggests that the active internalization mechanism may be partially blocked, and a small portion of CQDs was internalized by passive penetration.

The endocytosis of CQDs-3 was, in addition, quantitatively evaluated using flow cytometry by treating Huh-7 cells with 100 μg mL⁻¹ of CQDs-3 for 1 h at 4 °C and for 1, 3, and 6 h at 37 °C (Figure S2). The excitation fluorescence of CQDs-3 at 488 nm allowed analysis of CQDs intracellularly. A progressive shift in the cell population toward higher fluorescence values was observed with a subsequent increase of time incubation due to the time-dependent cellular uptake likely through endocytosis. Lower fluorescence intensity was observed upon incubation at 4 °C for 1 h, where the active uptake process is blocked. The low percentage of green cells (0.8%) observed after 1 h at 4 °C

suggests that only a very low quantity of CQDs-3 penetrates via passive uptake.

2.1.3. Antiviral Assay of First-Generation of Antiviral CQDs. The antiviral activity of CQDs-1, CQDs-3, and CQDs-4 was evaluated on Huh-7 cells monolayers, infected with HCoV-229E-Luc (Figure 4A). Addition of CQDs-1 after 1 h infection and further incubation for 6 h at 37 °C shows no inhibition of infection. This contrasts to CQDs-3 where a concentration-dependent virus inactivation is observed with an estimated EC₅₀ = 52 ± 8 μg mL⁻¹ (Figure 4B). Addition of mannose to CQDs-3 results in a complete loss of antiviral activity of the latter at low particle concentrations, with some antiviral activity above 50 μg mL⁻¹ CQDs. These data reveal two important findings. First, it highlights that boronic acid functions, where the mode of action is the selective and reversible formation of tetravalent complexes with *cis*-diols and thus glycan units,²⁴ are interacting with HCoV-229E. CQDs-3 are in this context speculated to be pseudolectins, targeting the S protein of HCoV-229E via a lectin–carbohydrate binding mechanism, similar to that of the oligomannose-specific lectin Griffithsin.²⁵ Thus, the presence of mannose is blocking the antiviral activity in favor of this mechanistic behavior. The presence of some antiviral activity of the mannose saturated CQDs-3 might be due to the presence of the triazole function on the particles' surface. Indeed, the control particles CQDs-4, bearing no boronic acid function but a triazole ring, display some antiviral activity, even though largely decreased when compared to CQDs-3.

2.2. Second-Generation of CQDs Inhibitors of Host Cell Infections by HCoV-229E Coronavirus. **2.2.1. Formation and Characterization of CQDs-5–7.** With the aim to validate if boronic acid functions can be formed directly on CQDs, hydrothermal carbonization of phenyl boronic acid and 4-aminophenylboronic acid was performed resulting in CQDs-5 and CQDs-6, respectively (Figure 5A). As control, hydrothermal carbonization of aniline and polyethylene glycol (PEG₆₀₀), both lacking boronic acid functions, was conducted. Unfortunately, several attempts to prepare CQDs from aniline as a starting material failed (see the Supporting Information for experimental details).

The TEM images of CQDs-5–7 are seen in Figure 5B. CQDs-5 have an average diameter of 9.2 ± 0.3 nm, somehow larger than CQDs-6 with an average size distribution of 7.6 ± 0.2 nm (Table 2). The particles formed from PEG (CQDs-7) display a spherical shape with an average diameter of 8.0 ± 0.2 nm.

The XRD diffractograms (see Figure S3A) display broad diffraction peaks centered at 21.3° for CQDs-5, 22.6° for CQDs-6, and 22.1° for CQDs-7, corresponding to an interlayer spacing of 0.42 nm (CQDs-5), 0.40 nm (CQDs-6), and 0.39 nm (CQDs-7). The UV/vis absorption spectra of the CQDs are depicted in Figure S3B. The absorption shoulders at 250–300 nm correspond to a typical absorption of an aromatic π system, in accordance with the literature data.²⁶ The CQDs exhibit different fluorescence quantum yields (QY) of 0.03 (CQDs-5),

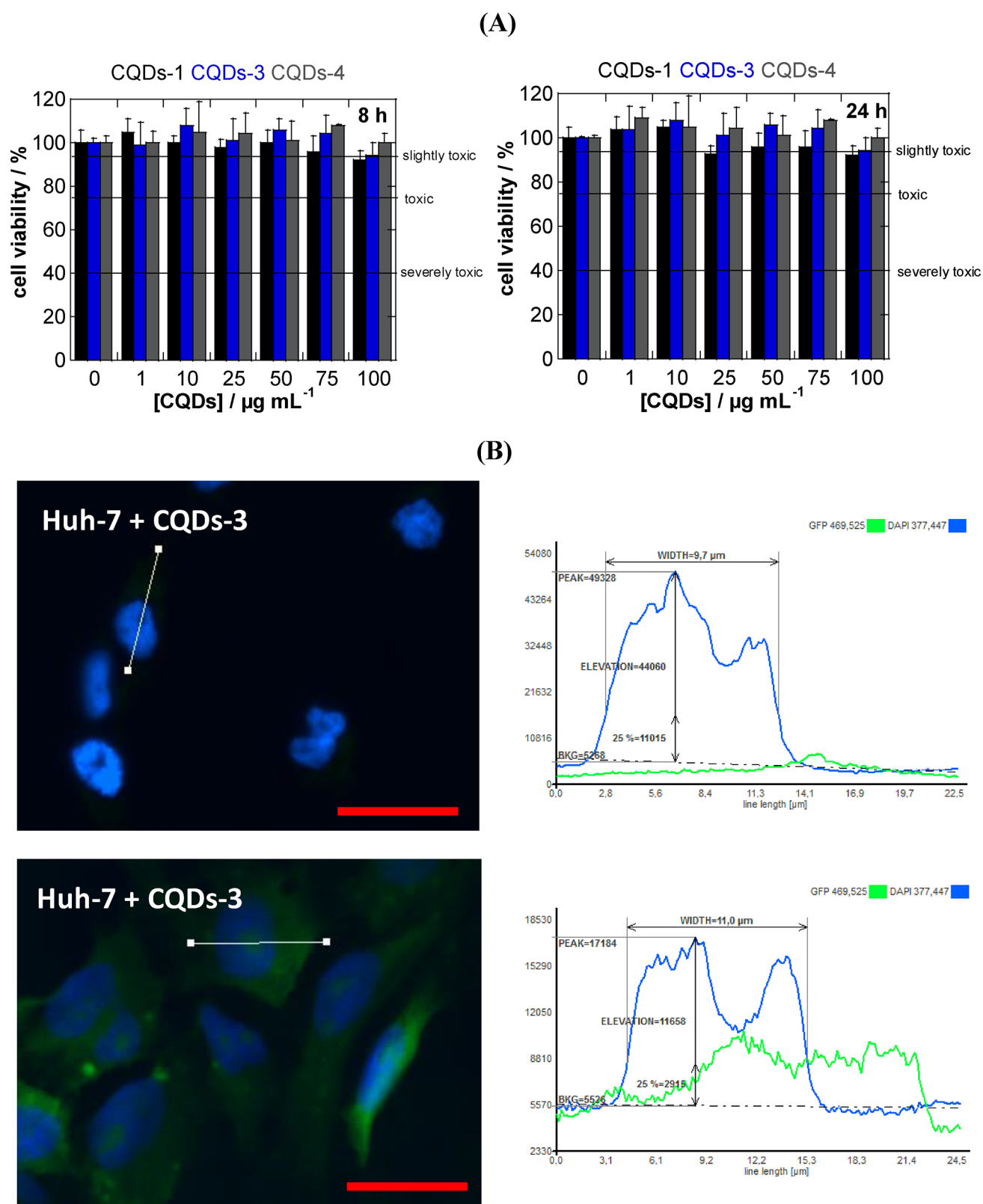


Figure 3. Characterization of postfunctionalized CQDs: (A) Viability of Huh-7 cells treated with the different CQDs. Huh-7 cells were grown in 96-well plates (15×10^3 cells/well) with $100 \mu\text{L}$ of culture medium containing increasing concentration of CQDs for 8 h (left) and 24 h (right). The results, expressed as percentage of viability, are the mean value of two independent experiments with each treatment performed in triplicate. Negative control: without CQDs. (B) Fluorescence microscopy of Huh-7 cells treated with $100 \mu\text{g mL}^{-1}$ of CQDs-3 for 1 h at 4°C (upper) and 37°C (lower). The blue signal corresponds to the nuclei stained with Hoechst 33342, while the green signal is attributed to CQDs-3. Scale bars = $50 \mu\text{m}$.

260 0.05 (CQDs-6), and 0.09 (CQDs-7) (Figure S3C). The wave-
261 length-dependent fluorescence emission properties of the CQDs are

comparable (Figure S3D). The zeta potential and hydrodynamic 262
size of CQDs-5–7 are summarized in Table 2. Raman spectra of 263

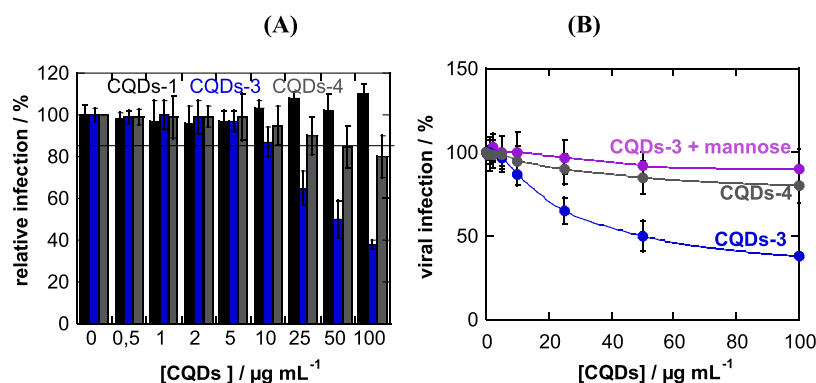


Figure 4. Viral infection inhibition in the presence of CQDs: (A) Viral inhibition using CQDs at various concentrations. Huh-7 cells (1.5×10^4 cells/well) were inoculated with HCoV-229E-Luc for 1 h (in atmosphere with 5% CO_2 at 37°C) in the presence or absence of different CQDs in medium without FBS for 1 h. Afterward, the inoculum was removed and replaced with DMEM with FBS for 6 h. Cells were lysed, and luciferase activity was quantified. The results are expressed as percentage of infection normalized to the control without CQDs, which is expressed as 100% infection. Data are means of two independent experiments with each treatment performed in triplicate. (B) Determination of EC_{50} for CQDs-3 and CQDs-4, and effect of viral inhibition using CQDs-3 after incubation with mannose (2:1) overnight at 4°C .

the CQDs-5–7 (Figure S3E) remain indifferent to that of CQDs-1 displaying the characteristic G and D band with $I_D/I_G = 0.93 \pm 0.15$ for all particles.

The chemical composition of the particles was thus further assessed using X-ray photoelectron spectroscopy and ^{11}B NMR. The XPS survey spectra of different CQDs (Table 2) indicate the presence of C_{1s} , O_{1s} , N_{1s} , and B_{1s} in agreement with the chemical composition of the particles. Deconvolution of the C_{1s} XPS spectrum of CQDs-5 reveals bands located at 284.3 eV ($\text{C}=\text{C}$, sp^2), 285.1 eV ($\text{C}-\text{H}$, $\text{C}-\text{B}$), and a small contribution centered at 287.0 eV ($\text{C}=\text{O}$) (Figure 5C). The boron content is lower than that reported by Shen and Xi,²⁷ but comparable to that reported by Wang et al.²⁸ This indicates that some of the phenylboronic acid groups were carbonized under our experimental conditions. The low B content might also indicate doping rather than the presence of boronic acid function. CQDs-6 particles depict bands at 284.3 eV ($\text{C}=\text{C}$, sp^2), 285.2 eV ($\text{C}-\text{H}$, $\text{C}-\text{B}$), 287.3 eV ($\text{C}=\text{O}$), and a band at 290.3 eV due to $\text{O}-\text{C}=\text{O}$ functions. In the case of CQDs-7, the C_{1s} XPS spectrum comprises three different carbon features: the graphitic $\text{C}=\text{C}$ at 283.4 eV, 284.9 eV ($\text{C}-\text{H}$), and 286.4 eV ($\text{C}-\text{O}$, $\text{C}-\text{N}$). Analysis of the N_{1s} high-resolution spectrum of CQDs-5 reveals the presence of surface $-\text{NH}_2$ groups (Figure 5D).

The FTIR spectra (Figure 5E) of CQDs-5–7 exhibit a distinct band at 3465 cm^{-1} attributed to the stretching vibration of $-\text{OH}$ groups and bands at around 2874 and 2924 cm^{-1} due to CH_2 stretching bands. The sharp band at 1618 cm^{-1} is assigned to graphitic $\text{C}=\text{C}$, and the $\text{C}-\text{H}$ deformation mode is seen at 1460 cm^{-1} . The $\text{C}=\text{O}$ band at ~ 1780 – 1650 cm^{-1} is also visible in all cases. In the case of CQDs-6, the band at 1090 cm^{-1} might be due to $\text{C}-\text{B}$ stretching modes. This band is less defined in the case of CQDs-5, which might underline doping rather than the presence of boronic acid functions. The FTIR spectrum of CQDs-7 displays the $\text{C}-\text{O}-\text{C}$ bands of the PEG units at 1043 cm^{-1} .

CQDs-5–7 exhibited a negative zeta potential in water (pH 7.4) at room temperature and showed excellent long-term stability even in biological medium such as Dulbecco's Modified Eagle's medium (M) (Figure 5F).

The cytotoxicity of CQDs-5–7 (Figure 6) is comparable to the CQDs discussed before (Figure 3), with CQDs-6 being slightly more toxic at concentrations $>25\text{ }\mu\text{g mL}^{-1}$ after 24 h incubation. This might be due to the presence of NH_2 groups on

these particles. The uptake mechanism of these particles was comparable and is exemplified using CQDs-6 in Figure S4. Because of low intrinsic fluorescence CQDs-6 particles, they were labeled with fluorescein-NHS.

2.2.2. Antiviral Assay of the Second-Generation of CQDs-5–7. Addition of CQDs-7 after 1 h infection and further incubation for 6 h at 37°C showed no inhibition of infection (Figure 7A), indicating that these particles are not interfering with HCoV-229E-Luc entry or replication. CQDs-5 and CQDs-6 display a concentration-dependent virus inactivation. The dose-response curve (Figures 7B) reveals that the effective concentration to achieve 50% inhibition (EC_{50}) against HCoV-229E-Luc infection is $5.2 \pm 0.7\text{ }\mu\text{g mL}^{-1}$ for CQDs-6 and $11.6 \pm 1.1\text{ }\mu\text{g mL}^{-1}$ for CQDs-5. Surprisingly, addition of mannose did not result in a loss of the antiviral activity (Figure 7C), as observed previously for CQDs-3.

Performing ^{11}B NMR analysis of CQDs-5 and CQDs-6 (Figure 7D) and comparing the obtained spectra to those of the respective starting materials, 4-aminophenylboronic acid and phenyl boronic acid (Figure 7E), reveal large differences in chemical composition. 4-Aminophenylboronic acid and phenyl boronic both exhibit a strong signal at around 29 ppm, in accordance with literature data for $-\text{B}(\text{OH})_2$ functions.^{29,30} The small signal at about 20 ppm arises most likely from residual $\text{B}(\text{OR})_3$ often used in boronic acid synthesis.³¹ The ^{11}B NMR spectra of CQDs-5 and CQDs-6 display, however, peaks at 13 ppm (CQDs-5) and a band at 10 ppm with a shoulder at 12 ppm for CQDs-6. This means that boron was incorporated through doping rather than surface functionalization, during the hydrothermal reaction. Indeed, one-pot solvothermal synthesis using aminophenylboronic acid precursor was reported by Wang et al. to result in N and B codoped CQDs.³² They indeed reported the presence of 0.7 at. % B by XPS comparable to the amount obtained here (Table 2).

2.3. Mechanism of Action. We further investigated the mechanism of action of CQDs-3 and CQDs-6 on viral infection by performing a time-of-addition assay. CQDs (at $10\text{ }\mu\text{g mL}^{-1}$) were added at different time points during infection, as represented in Figure 8A. As expected, a strong inhibition of infection was observed when CQDs were added after 1 h inoculation. Moreover, the inhibition activity of CQDs was stronger when the nanoparticles were added during the entry step, that is, 30 minutes before and after inoculation and during inoculation.

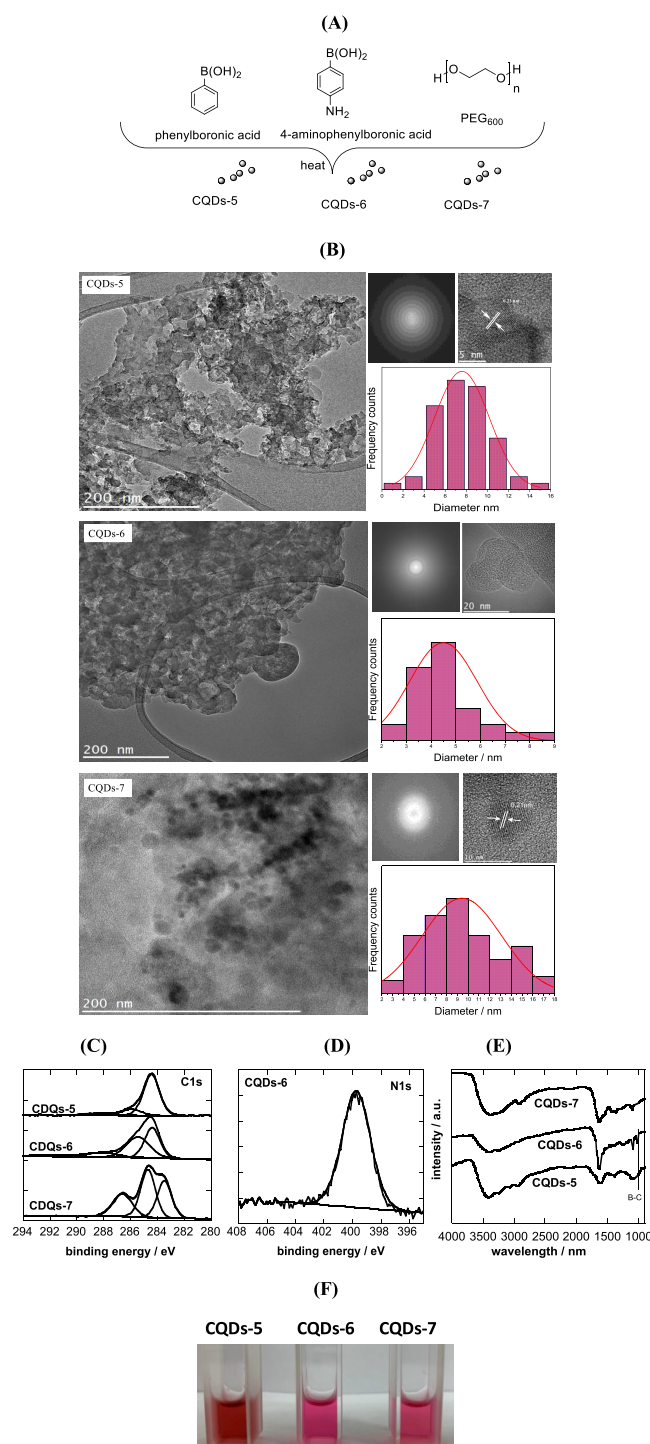


Figure 5. Chemical composition of the CQDs-5–7: (A) Schematic representation of the hydrothermal carbonization of different organic precursors for the synthesis of CQDs-5–7; (B) TEM, magnified TEM, and size distribution histograms of CQDs-5–7; (C) C_{1s} high-resolution XPS spectrum of CQDs-5–7; (D) N_{1s} high-resolution XPS spectrum of CQDs-6; (E) FTIR spectra of CQDs-5–7; and (F) photographs of CQDs-5–7 suspensions (1 mg mL^{-1}) after 1 month in Dulbecco's Modified Eagle's medium (M).

350 These results agree with our hypothesis of an interaction of
351 CQDs with HCoV-229E S protein, or an interaction of CQDs
352 with entry factors. Surprisingly, a strong inhibitory activity of
353 CQDs was also observed when they were added after 5.5 h after
354 the entry step, the replication step. The inhibition is not

355 significantly different for the entry step as compared to the
356 replication step. This suggests that, in addition to its major effect
357 on HCoV-229E entry, CQDs can also affect the genomic repli-
358 cation of this virus. This could potentially be explained by an
359 interaction between the CQDs and a cell surface protein leading
360 to signal transduction affecting viral replication, or by an inter-
361 action with cytosolic proteins as CQDs are internalized.

362 To determine if CQDs are interacting directly with viral parti-
363 cles, HCoV-229E-Luc was incubated with CQDs at $10 \mu\text{g mL}^{-1}$
364 for 30 min at 37°C before inoculation. The inoculum was
365 diluted 10 times, leading to a final concentration of CQDs of
366 $1 \mu\text{g mL}^{-1}$, and infection assay was performed. In parallel, Huh-7
367 cells were inoculated with HCoV-229E-Luc in the presence of
368 CQDs at 1 or $10 \mu\text{g mL}^{-1}$. The inoculum titers were kept
369 constant in the different conditions. The results showed that the
370 preincubation of the virus with CQDs at high concentration
371 does not impair HCoV-229E infection, meaning that CQDs are
372 not interacting with the particles before infection (Figure 8B).
373 Taken together, our results are in favor of an interaction of
374 CQDs with cellular factors that may explain their antiviral effects
375 at different steps of infection.

3. CONCLUSION

376 The viral infection cycle produces important biological and
377 structural changes in the host cell, resulting in cell damage. The
378 possibility to interfere with viral attachment to cells as well as
379 viral replication to reduce viral infection and spreading is an
380 appropriate antiviral approach. We presented here the antiviral
381 performance of seven different CQDs with their main features
382 summarized in Table 3. Three of these CQDs (CQDs-3, -5, -6)
383 were shown to interfere significantly with HCoV-229E-Luc
384 infection in a concentration-dependent manner, while CQDs-4
385 showed a very moderate antiviral activity. The estimated EC_{50}
386 value decreased considerable from CQDs-3, boronic acid-
387 modified quantum dots, derived from ethylenediamine/citric
388 acid as carbon precursors ($EC_{50} = 52 \pm 8 \mu\text{g mL}^{-1}$) to $5.2 \pm$
389 $0.7 \mu\text{g mL}^{-1}$ in the case of CQDs-6. While the presence of
390 boronic acid functions proved to be vital for covering CQDs-3
391 with antiviral activity, CQDs-5 and CQDs-6 did not carry a
392 substantial amount of boronic acid functions, as revealed by ^{11}B
393 NMR and validated by mannose addition experiments. These
394 findings reveal the complex nature of identifying viral inhibitors
395 for human coronaviruses such as HCoV-229E-Luc. Mechanistic
396 studies suggest that the particles are acting at the early state of
397 virus infection through the inhibition of entry that could be due
398 to inhibition of protein S-receptor interaction with the host cell
399 membrane. All different particles interfere in addition with the
400 viral replication step, something less common. These results are
401 extremely encouraging to replace currently used antiviral agents
402 such a ribavirin and IFN known to have major side effects such as
403 confusion, short-term memory loss, deficits in executive
404 functions, as well as extrapyramidal effects. Further experimental
405 confirmations are required if this approach can be extrapolated
406 to other coronaviruses, notably to the clinically relevant MERS-
407 CoV, to validate the potential of these nanostructures as
408 alternative anti-MERS therapeutics and approaches to confront
409 this severe and life-threatening disease. Also, how such particles
410 work in vivo has to be shown in the future.

4. EXPERIMENTAL SECTION

411 **4.1. Materials.** Citric acid, ethylenediamine, 4-aminophenylboronic
412 acid, phenylboronic acid, poly(ethylene glycol) (PEG600, molecular
413 weight 570–630), *N*-(3-(dimethylamino)propyl)-*N'*-ethylcarbodiimide

Table 2. Physico-chemical Characteristics of the CQDs-5–7

CQDs	ζ (mV) ^a	size (nm)	hydrodynamic size (nm) ^b	PDI	C _{1s} ^c (at. %)	O _{1s} (at. %)	N _{1s} (at. %)	B _{1s} (at. %)
CQDs-5	-20.0 ± 5.5	7.6 ± 0.2	13 ± 1.8	0.14 ± 0.09	77.4	21.7		0.9
CQDs-6	-41.2 ± 1.0	9.2 ± 0.3	12 ± 0.2	0.11 ± 0.06	69.4	21.5	7.4	1.7
CQDs-7	-39.2 ± 1.5	8.0 ± 0.2	13 ± 3.1	0.28 ± 0.34	60.8	39.2		

^a ζ , zeta potential; PDI, polydispersity index. ^bThe hydrodynamic size was recorded at 37 °C. ^cXPS was used to determine the atomic percentage of the elements, respectively.

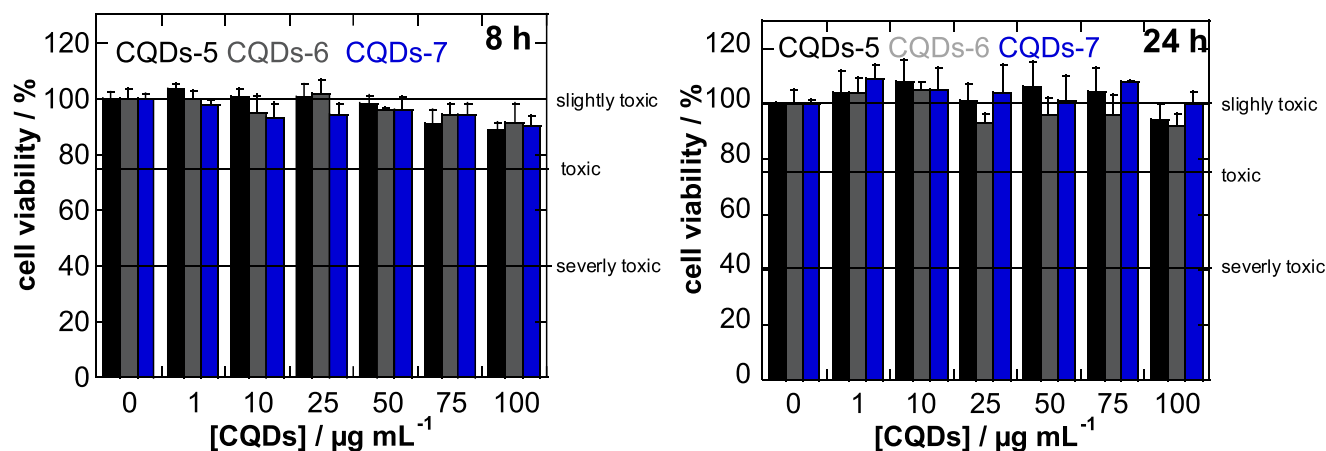


Figure 6. Cell viability of CQDs-5–7: Viability of Huh-7 cells grown in 96-well plates (15×10^3 cells/well) with 100 μ L of culture medium containing increasing concentration of CQDs-5–7 labeled for 8 and 24 h. The results, expressed as percentage of viability, are the mean value of two independent experiments with each treatment performed in triplicate. Negative control: without CQDs.

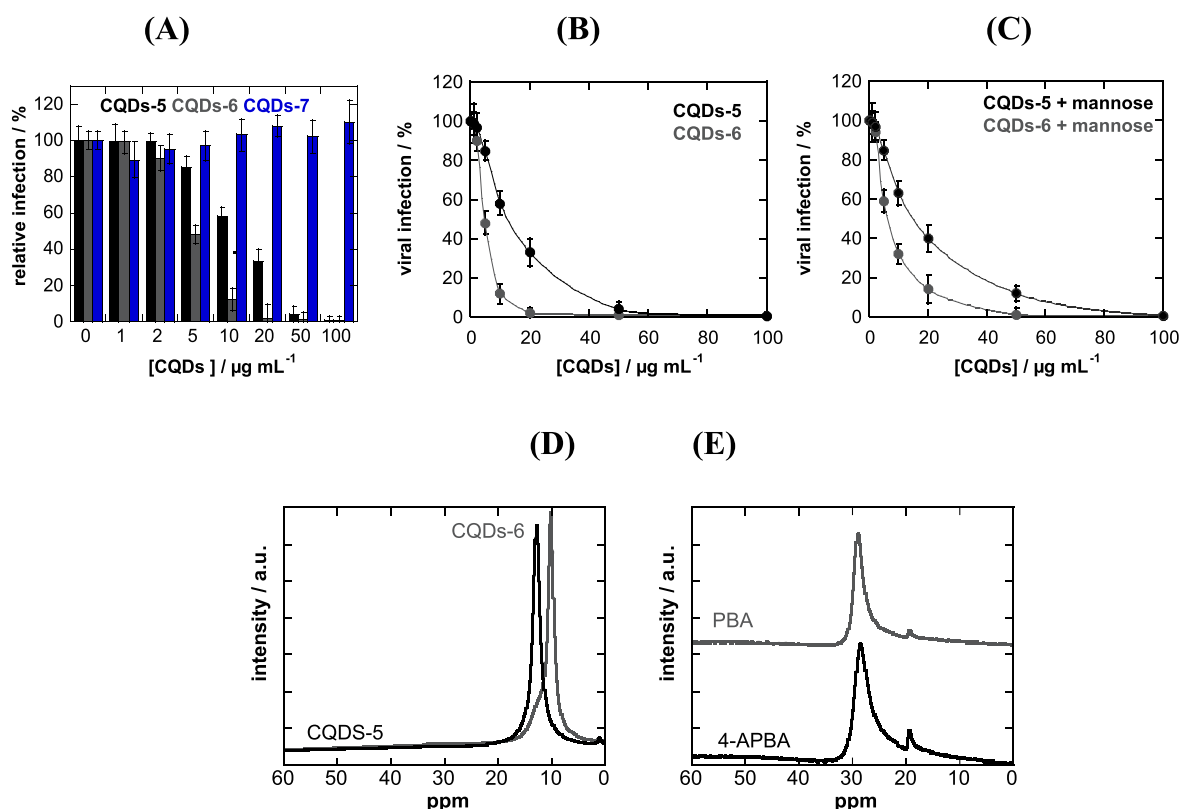


Figure 7. Viral infection inhibition in the presence of CQDs-5–7: (A) Viral inhibition using CQDs-5–7 at various concentrations. Huh-7 cells (1.5×10^4 cells/well) were inoculated with HCoV-229E-Luc for 1 h (in atmosphere with 5% CO₂ at 37 °C) in the presence or absence of different CQDs in medium without FBS for 1 h. Afterward, the inoculum was removed and replaced with DMEM with FBS for 6 h. Cells were lysed, and luciferase activity was quantified. The results were expressed as percentage of infection normalized to the control without CQDs, which is expressed as 100% infection. Data are means of two independent experiments with each treatment performed in triplicate. (B) Determination of EC₅₀ for CQDs-5 and CQDs-6. (C) Viral inhibition using CQDs-5 and CQDs-6 after incubation with mannose (2:1) overnight at 4 °C. (D) ¹¹B NMR spectra of CQDs-5 and CQDs-6 prepared by hydrothermal method from phenyl boronic acid (PBA) and 4-aminophenylboronic acid (4-APBA) precursors, respectively. (E) ¹¹B NMR spectra of 4-aminophenylboronic acid (4-APBA) and phenyl boronic acid (PBA) starting materials.

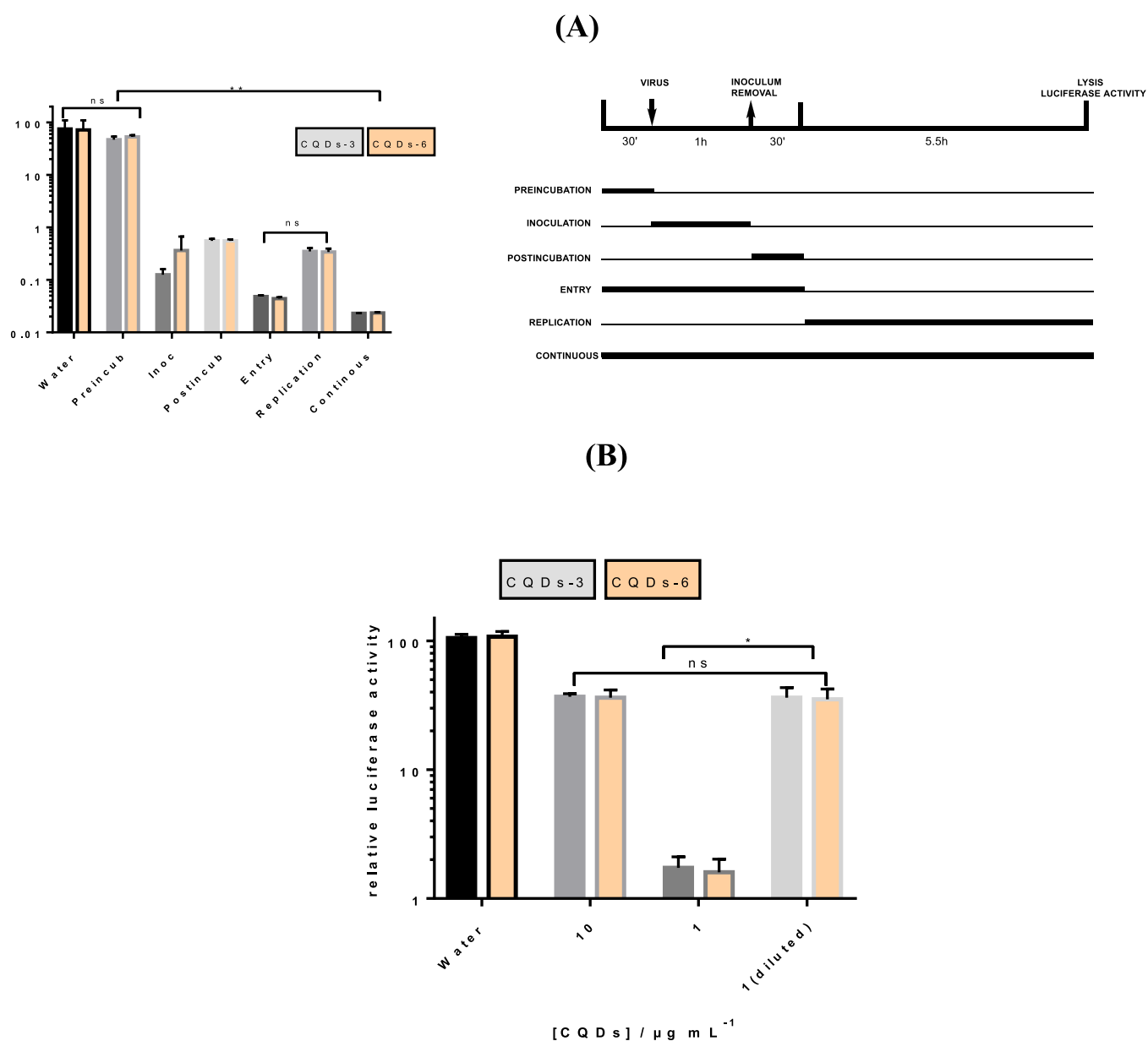


Figure 8. Time-of-addition assay of CQDs-3 and -6 during HCoV-229E infection. (A) CQDs at $10 \mu\text{g mL}^{-1}$ were added at different time points during infection of Huh-7 cells with HCoV-229E-Luc as shown below the graph. Cells were lysed, and luciferase activity was quantified. Results are representative of three experiments performed in triplicate. Error bars represent SD of three independent values. (B) Virus HCoV-229E-Luc was preincubated with CQDs at $10 \mu\text{g mL}^{-1}$ for 30 min at 37°C . The mixture was diluted 10 times in culture medium leading to a final concentration of CQDs of $1 \mu\text{g mL}^{-1}$, and inoculated on Huh-7 cells for 1 h. In parallel, Huh-7 cells were inoculated with HCoV-229E-Luc in the presence of CQDs at 1 and $10 \mu\text{g mL}^{-1}$ for 1 h. Cells were lysed 7 h postinfection and luciferase activity quantified. Results are means of three experiments performed in triplicate. Error bars represent means of three independent values. Statistic evaluation (confidence interval of 95%, ns ($p > 0.99$); * ($p < 0.1$); ** ($p < 0.01$)).

414 hydrochloride, *N*-hydroxysuccinimide, propargyl alcohol, 4-pentynoic
415 acid, copper sulfate pentahydrate, L-ascorbic acid, and sodium hydrox-
416 ide were purchased from Sigma-Aldrich. The dialysis membranes were
417 supplied by Spectrum Laboratories.

418 **4.2. Synthesis of Functional Carbon Quantum Dots (CQDs).**
419 *CQDs-1*. Particles were synthesized following a method similar to that
420 reported by Zhu et al.³³ (see Supporting Information S11 for more
421 details). The details about the characterization instruments can be
422 found in Supporting Information S12.

423 *CQDs-2*. Azide-terminated CQDs-2 were obtained from CQDs-1 by
424 the use of carbodiimide chemistry. To a solution of 2-azidoacetic acid
425 (1 mg mL^{-1} , 0.1X PBS) was added an equimolar amount of EDC-HCl
426 and NHS, and the solution was stirred for 20 min to activate the
427 carboxyl group. To this solution was added CQDs-1 (1 mg mL^{-1} , 0.1X
428 PBS) in a 1:2 volume ratio (v/v). The reaction was carried out for 5 h at

room temperature, and the resulting solution was then dialyzed against 429
Milli-Q water using cellulose ester dialysis membrane for 24 h (Biotec 430
CE no. 131093, molecular weight cutoff 500–1000 Da) to remove 431
unreacted material. 432

CQDs-3. CQDs-2 were further reacted with “clickable” phenyl boronic 433
acid derivative 4-[(1-oxo-4-pentyn-1-yl)amino]phenylboronic acid, 434
synthesized as reported previously.³⁴ For this, CQDs-2 (1 mg mL^{-1} , 435
5 mL) were mixed with 4-[(1-oxo-4-pentyn-1-yl) amino] phenyl- 436
boronic acid (2 mM), copper sulfate pentahydrate ($200 \mu\text{M}$), and 437
ascorbic acid ($300 \mu\text{M}$). The reaction mixture was stirred for 24 h at 438
room temperature. EDTA was added to the mixture prior to dialysis 439
(SpectraPor 1, pore size: 1000 Da) against Milli-Q water for 48 h. 440

CQDs-4. CQDs-2 were further reacted with commercially available 441
propargyl alcohol. For this, CQDs-2 (1 mg mL^{-1} , 5 mL) were mixed 442
with propargyl alcohol (2 mM), copper sulfate pentahydrate ($200 \mu\text{M}$), 443

Table 3. Summary of the Main Features of CQDs-1–7

CQDs	size (nm)	charge	functions	antiviral	EC ₅₀ /μg mL ^{-1a}
CQDs-1	4.5 ± 0.2	-9.9	NH ₂ , COO ⁻	-	
CQDs-2	5.5 ± 0.3	-7.9	N ₃	-	
CQDs-3	6.3 ± 0.4	-15.9	triazole, R-B(OH) ₂	++	52 ± 8
CQDs-4	6.5 ± 0.4	-15.9	triazole, OH	+	n.d.
CQDs-5	7.6 ± 0.2	-20.0	R-B(OH) ₂	+++	11.6 ± 1.1
CQDs-6	9.2 ± 0.3	-41.2	R-B(OH) ₂ , NH ₂	++++	5.2 ± 0.7
CQDs-7	8.0 ± 0.3	-39.2	PEG	-	

^and, not determinable.

444 and ascorbic acid (300 μM). The reaction mixture was stirred for 24 h at
445 room temperature. EDTA was added to the mixture prior to dialysis
446 (SpectraPor 1, pore size: 1000 Da) against Milli-Q water for 48 h.

447 CQDs-5 and CQDs-6. Particles were prepared according to the
448 protocol recently described by us.¹²

449 CQDs-7. Particles were prepared in a manner similar to that for
450 CQDs-2 by dissolving PEG600 (200 mg) in water (20 mL) and
451 adjusting the pH to 9.0 by adding NaOH (0.5 M). The solution was
452 degassed with nitrogen gas during 1 h to remove dissolved oxygen and
453 heated in a Teflon-lined autoclave chamber (125 mL – acid digestion
454 vessel no. 4748, Parr, France) for 72 h at 120 °C. After being cooled to
455 room temperature, the solution was dialyzed against water for 24 h with
456 water being changed every 6 h (SpectraPor 1, pore size: 3500 Da).

457 **4.3. Biological Assays. Cell and Toxicity Assay.** The Huh-7
458 hepatocarcinoma cell line was cultured and maintained in Dulbecco's
459 Modified Eagle's medium (DMEM, Gibco) supplemented with 10%
460 fetal bovine serum (FBS, Gibco) and 1% penicillin-streptomycin
461 (Gibco) in a humidified incubator at 37 °C and 5% CO₂. Cells were
462 seeded at a density of 15 × 10³ cells/well in a 96-well plate and grown
463 for 24 h before assay. The culture medium was replaced with a fresh
464 medium that contains increasing concentrations of CQDs for 2 and 8 h
465 from 1 to 100 μg mL⁻¹. The old medium was then aspirated, and cells
466 were washed with PBS. The cell viability was evaluated using resazurin
467 cell viability assay. Briefly, 100 mL of the resazurin solution (11 μg mL⁻¹)
468 in DMEM/10% FBS was added to each well, and the plate was incu-
469 bated for 4 h in the humidified incubator. The fluorescence emission of
470 each well was measured at 593 nm (20 nm bandwidth) with an excita-
471 tion at 554 nm (18 nm bandwidth) using a Cytation 5 Cell Imaging
472 Multi-Mode Reader (BioTek Instruments SAS, France). Each con-
473 dition was replicated three times, and the mean fluorescence value of
474 nonexposed cells was taken as 100% cellular viability.

475 **Fluorescent Labeling of CQDs: Uptake Mechanism.** To study the
476 uptake mechanism of the particles into cells, CQDs were dissolved in
477 PBS buffer (pH 7.4) at the concentration of 2 mg mL⁻¹. Fluorescein-
478 NHS was dissolved in DMF (10 mg mL⁻¹). A solution of CQDs-5 was
479 cooled to 0 °C, and 10 μL of freshly prepared fluorescein-NHS solution
480 was added. The reaction was stirred on ice for another 3 h. To remove
481 the excess of the fluorescein dye, a Sephadex G-25 PD-10 desalting
482 column was used. Cells were seeded at a density of 15 × 10⁴ cells/well in
483 a 24-well plate with sterile coverslips at the bottom and grown for 24 h
484 before assay. The culture medium was replaced with a fresh medium
485 that contained 100 μg mL⁻¹ of CQDs. After 1 h incubation at 4 and
486 37 °C, the Huh-7 cells were washed with PBS (three times), fixed with
487 4% paraformaldehyde for 10 min at room temperature, and then stained
488 with 10 μg mL⁻¹ Hoechst 33342 in PBS for 10 min at room temperature
489 in the dark. After being washed with PBS, the coverslips were mounted
490 on glass slides and recorded using a Cytation 5 Cell Imaging Multi-
491 Mode Reader (BioTek Instruments SAS, France) equipped with 40×
492 objective (Plan Fluorite WD 2.7 NA 0.6). The fluorescence images
493 were acquired with the same exposure using DAPI (377/447 nm) and
494 GFP (469/525 nm) excitation/emission filter sets. All of the images
495 were processed using Gen5 Image+ software.

496 For cellular uptake, cells were seeded at a density of 15 × 10⁴ cells/well
497 in a six-well plate and grown for 48 h before assay. The culture medium
498 was replaced with a fresh medium that contained 100 μg mL⁻¹ of

CQDs. After 1 h incubation at 4 °C and 1, 3, and 6 h incubation at
37 °C, the Huh-7 cells were washed with PBS (three times) and
collected by trypsinization. The cells suspensions were resuspended in
PBS/PFA 0.5% and analyzed through a flow cytometer (BD LSR
Fortessa) with FITC channel. The data were collected (10⁴ cells per
sample) and analyzed using BD FACSDiva 8.0.1 software.

Antiviral Assay: HCoV-229E-Luc. We used a modified HCoV-229E
containing a renilla luciferase reporter gene HCoV-229E-Luc. The viral
stocks were produced in Huh-7 cells. Huh-7 cells were infected with a
prestock of HCoV-229E-Luc in flasks. After 5 days, the supernatants of
flasks were collected. For infection assay, Huh-7 cells, 15 000/well
seeded in 96-well plate, were inoculated with HCoV-229E-Luc at a
multiplicity of infection (MOI) of 1 during 1 h at 37 °C in DMEM
without serum, and then the inoculum was removed and cells were
incubated in complete culture medium for 6 h at 37 °C. CQDs were
added to cells during the 1 h of infection. Cells were lysed in 20 μL of
Renilla Lysis Buffer (Promega, Madison, WI) and luciferase activity
quantified using a Renilla Luciferase Assay System kit (Promega,
Madison, WI) as recommended by the manufacturer and a Tristar LB
941 luminometer (Berthold Technologies, Bad Wildbad, Germany).
To measure EC₅₀, dose–response experiment was performed with
CQDs added at different concentrations during inoculation step and
postinoculation step. For time-of-addition assays, CQDs were added at
different time points at 10 μg mL⁻¹. For all experiments, water was used
as a control because CQDs are diluted in water.

Statistical Analysis. The statistical test used is a Mann–Whitney
nonparametric with a confidence interval of 95%. The data were
analyzed using GraphPad Prism (version 5.0b) by comparison between
treated and untreated groups (DMSO control). *P* values of 0.05 were
considered to be significantly different from the control.

■ ASSOCIATED CONTENT

Supporting Information

The Supporting Information is available free of charge on the
ACS Publications website at DOI: 10.1021/acsami.9b15032.

Synthesis of functional cation quantum dots (CQDs-1,
CQDs-5, CQDs-6) as well as the synthesis of CQDs from
aniline (S1); description of methods used for the
characterization of CQDs (S2); wavelength-dependent
fluorescence emission properties of the different CQDs
(Figure S1); Raman and some XPS high resolution (N_{1s}
XPS of CQDs-2 and CQDs-3; C_{1s} of CQDs-7; N_{1s} of
CQDs-7 (Figure S2)); flow cytometry analysis of cellular
uptake of CQDs in Huh-7 cells treated with 100 μg mL⁻¹
of CQDs-3 for 1 h at 4 °C and 1, 3, and 6 h at 37 °C
(Figure S3); and fluorescence microscopy of Huh-7 cells
treated with 100 μg mL⁻¹ of CQDs-5 labeled with
fluorescein for 1 h at 4 °C (upper) and 37 °C (lower),
with the blue signal corresponding to the nuclei stained
(Figure S4) (PDF)

■ AUTHOR INFORMATION

Corresponding Authors

*E-mail: jean.dubuisson@ibl.cnrs.fr.

*E-mail: sabine.szunerits@univ-lille.fr.

ORCID

Alexandre Barras: 0000-0003-2821-7079

Emerson Giovanelli: 0000-0001-9097-9301

Nils Metzler-Nolte: 0000-0001-8111-9959

Rabah Boukherroub: 0000-0002-9795-9888

Sabine Szunerits: 0000-0002-1567-4943

Notes

The authors declare no competing financial interest.

560 ■ ACKNOWLEDGMENTS

561 Financial support from the Centre National de la Recherche
562 Scientifique (CNRS), the University of Lille, the Hauts-de-
563 France region, the CPER "Photonics for Society", the Agence
564 Nationale de la Recherche (ANR), and the EU union through
565 the Marie Skłodowska-Curie action (H2020-MSCA-RISE-2015,
566 PANG-690836) is gratefully acknowledged. Research work is
567 supported by the Belgian F.R.S. – FNRS project SELFPHON.
568 We thank Volker Thiel for providing us with HCoV-229E-Luc
569 virus. We thank the Flow Core Facility – BioImaging Center
570 Lille (F-59000 Lille, France) for providing the technical
571 environment to perform flow cytometry analysis. Marc Bria is
572 thanked for help in recording the ¹¹B NMR spectra.

573 ■ REFERENCES

574 (1) Nii-Trebi, N. I. Emerging and Neglected Infectious Diseases:
575 Insights, Advances, and Challenges. *BioMed Res. Int.* **2017**, *2017*, 1–15.
576 (2) [http://www.who.int/csr/research-and-development/meeting-
577 report-prioritization.pdf](http://www.who.int/csr/research-and-development/meeting-report-prioritization.pdf) (accessed 16 September 2019).
578 (3) Al Hajjar, S.; Ziad A. Memish, Z. A.; McIntosh, K. Middle East
579 Respiratory Syndrome Coronavirus (MERS-CoV): A Perpetual
580 Challenge. *Ann. Saudi Med.* **2013**, *33*, 427–436.
581 (4) [http://www.emro.who.int/pandemic-epidemic-diseases/mers-
582 cov/mers-situation-update-november-2017.html](http://www.emro.who.int/pandemic-epidemic-diseases/mers-cov/mers-situation-update-november-2017.html) (accessed 16 Septem-
583 ber 2019).
584 (5) Mo, Y.; Fisher, D. A Review of Treatment Modalities Of Middle
585 Respiratory Syndromes. *J. Antimicrob. Chemother.* **2016**, *71*, 3340–
586 3350.
587 (6) Uyeki, T. M.; Erlandson, K. J.; Korch, G.; O'Hara, M.; Wathen,
588 M.; Hu-Primmer, J.; Hojvat, S.; Stemmy, E. J.; Donabedian, A.
589 Development of Medical Countermeasures to Middle East Respiratory
590 Syndrome Coronavirus. *Emerging Infect. Dis.* **2016**, *22*, 1–6.
591 (7) Zumla, A.; Chan, J. F. W.; Azhar, E. I.; Hui, D. S. C.; Yuen, K.-Y.
592 Coronavirus-Drug Discovery and Therapeutic Options. *Nat. Rev. Drug*
593 *Discovery* **2016**, *15*, 327–347.
594 (8) Du, L.; Yang, Y.; Zhou, Y.; Lu, L.; Li, F.; Jiang, S. MERS-Cov Spike
595 Protein: A Key Target for Antivirals. *Expert Opin. Ther. Targets* **2017**,
596 *21*, 131–143.
597 (9) Lu, L.; Liu, Q.; Zhu, Y.; Chan, K.-H.; Qin, L.; Li, Y.; Wang, Q.;
598 Chan, J. F. W.; Du, L.; Yu, F.; Ma, C.; Ye, S.; Yuen, K.-Y.; Zhang, R.;
599 Jiang, S. Structures-Based Discovery Of Middle East Respiratory
600 Syndrome Coronavirus Fusion Inhibitor. *Nat. Commun.* **2014**, *5*
601 (3067), 1–15.
602 (10) Szunerits, S.; Barras, A.; Khanal, M.; Pagneux, Q.; Boukherroub,
603 R. Nanostructures for the Inhibition of Viral Infections. *Molecules* **2015**,
604 *20*, 14051–14081.
605 (11) Lim, S. Y.; Shen, W.; Gao, Z. Carbon Quantum Dots And Their
606 Applications. *Chem. Soc. Rev.* **2015**, *44*, 362–381.
607 (12) Barras, A.; Pagneux, Q.; Sane, F.; Wang, Q.; Boukherroub, R.;
608 Hober, D.; Szunerits, S. High Efficiency of Functional Carbon
609 Nanodots as Entry Inhibitors of Herpes Simplex Virus Type 1. *ACS*
610 *Appl. Mater. Interfaces* **2016**, *8*, 9004–9013.
611 (13) Fahmi, M. Z.; Sukmayani, W.; Qamariyah Khairunisa, S.;
612 Witaningrum, A. M.; Indriati, D. W.; Matondang, M. Q. Y.; Chang, J.-
613 Y.; Kotaki, T.; Kameokaf, M. Design of boronic acid-attributed carbon
614 dots on inhibits HIV-1 entry. *RSC Adv.* **2016**, *6*, 92996–93002.
615 (14) Du, T.; Liang, J.; Dong, N.; Liu, L.; Fang, L.; Xiao, S.; Ha, H.
616 Carbon Dots As Inhibitors Of Virus By Activation Of Type I Interferon
617 Response. *Carbon* **2016**, *110*, 278–285.
618 (15) Trippier, P. C.; Balzarini, J.; C. McGuigan, A. Phenylboronic-
619 Acid-Based Carbohydrate Binders As Antiviral Therapeutics: Bi-
620 sphenylboronic Acids. *Chem. Chemother.* **2011**, *21*, 129–142.
621 (16) Khanal, M.; Barras, A.; Vausseil, T.; Fénéant, L.; Boukherroub,
622 R.; Siriwardena, A.; Dubuisson, J.; Szunerits, S. Boronic Acid-Modified
623 Lipid Nanocapsules: A Novel Platform For The Highly Efficient
624 Inhibition Of Hepatitis C Viral Entry. *Nanoscale* **2015**, *7*, 1392–1402.

(17) Gupta, V.; Chaudhary, N.; Srivastava, R.; Sharma, G. D.; R. 625
Bhardwaj, R.; S. Chand, S. Luminescent Graphene Quantum Dots for 626
Organic Photovoltaic Devices. *J. Am. Chem. Soc.* **2011**, *133*, 9960– 627
9963. 628
(18) Yaoping, H.; Jing, Y.; Jiangwei, T.; Jun-Sheng, Y. How Do 629
Nitrogen-Doped Carbon Dots Generate From Molecular Precursors? 630
An Investigation Of The Formation Mechanism And A Solution-Based 631
Large-Scale Synthesis. *J. Mater. Chem. B* **2015**, *3*, 5608–5614. 632
(19) Hu, C.; Liu, Y.; Yang, Y.; Cui, J.; Huang, Z.; Wang, Y.; Yang, L.; 633
Wang, H.; Xiao, Y.; Rong, J. One-Step Preparation Of Nitrogen-Doped 634
Graphene Quantum Dots From Oxidized Debris Of Graphene Oxide. *J.* 635
Mater. Chem. B **2013**, *1*, 39–42. 636
(20) Wang, S.; Cole, I. S.; Zhao, D.; Li, Q. The Dual Roles Of 637
Functional Groups In The Photoluminescence Of Graphene Quantum 638
Dots. *Nanoscale* **2016**, *8* (14), 7449–7458. 639
(21) Kim, T. H.; White, A. R.; Sirdaarta, J. P.; Ji, W.; Cock, I. E.; St. 640
John, J.; Boyd, S. E.; Brown, C. L.; Li, Q. Yellow-Emitting Carbon 641
Nanodots and Their Flexible and Transparent Films for White LEDs. 642
ACS Appl. Mater. Interfaces **2016**, *8*, 33102–33111. 643
(22) Agalave, S. G.; Maujan, S. R.; Pore, V. S. Click Chemistry: 1,2,3- 644
Triazoles as Pharmacophores. *Chem. - Asian J.* **2011**, *6*, 2696–2718. 645
(23) Hilimire, T. A.; Chamberlain, J. M.; Anokhina, V.; Bennett, R. P.; 646
O, S.; Myers, J. R.; Ashton, J. M.; Stewart, R. A.; Featherston, A. L.; 647
Gates, K.; Helms, E. D.; Smith, H. C.; Dewhurst, S.; Miller, B. L. HIV-1 648
Frameshift RNA-Targeted Triazoles Inhibit Propagation of Repli- 649
cation-Competent and Multi-Drug-Resistant HIV in Human Cells. 650
ACS Chem. Biol. **2017**, *12*, 1674–1682. 651
(24) Yan, J.; Fang, H.; Wang, B. Boronolactams And Fluorescent 652
Boronolactams: An Examination Of The Detailed Chemistry Issues 653
Important For The Design. *Med. Res. Rev.* **2005**, *25*, 490–520. 654
(25) O'Keefe, B. R.; Giomarelli, B.; Barnard, D. L.; Shenoy, S. R.; 655
Chan, P. K. S.; McMahan, J. B.; Palmer, K. E.; Barnett, B. W.; 656
Meyerholz, D. K.; Wohlford-Lenane, C. L.; McCray, P. B. Broad- 657
Spectrum In Vitro Activity And In Vivo Efficacy Of The Antiviral 658
Protein Griffithsin Against Emerging Viruses Of The Family 659
Coronaviridae. *J. Virol.* **2010**, *84*, 2511–2521. 660
(26) Li, H.; He, X.; Kang, Z.; Huang, H.; Liu, J.; Lian, S.; 661
Tsang, C. H. A.; Yang, X.; Lee, S.-T. Water-Soluble Fluorescent Carbon 662
Quantum Dots and Photocatalyst Design. *Angew. Chem., Int. Ed.* **2010**, 663
49, 4430–4434. 664
(27) Shen, P.; Xia, Y. Synthesis-Modification Integration: One-Step 665
Fabrication of Boronic Acid Functionalized Carbon Dots for 666
Fluorescent Blood Sugar Sensing. *Anal. Chem.* **2014**, *86*, 5323–5329. 667
(28) Wang, Y.; Lu, L.; Peng, H.; Xu, J.; Wang, F.; Qi, R.; Xu, Z.; Zhang, 668
W. Multi-Doped Carbon Dots With Ratiometric Ph Sensing Properties 669
For Monitoring Enzyme Catalytic Reactions. *Chem. Commun.* **2016**, *52*, 670
9247–9250. 671
(29) De Moor, J. E.; Van Der Kelen, P. Studies On Trivalent Boron 672
Compounds II. Dipole Moment Measurements. *J. Organomet. Chem.* 673
1967, *9*, 23–29. 674
(30) Beachell, H. C.; Beistel, D. W. Nuclear Magnetic Resonance 675
Spectra of Phenylboronic Acids. *Inorg. Chem.* **1964**, *3*, 1028–1032. 676
(31) Good, C. D.; Ritter, D. M. Alkenylboranes. II. Improved 677
Preparative Methods and New Observations on Methylvinylboranes. *J.* 678
Am. Chem. Soc. **1962**, *84*, 1162–1166. 679
(32) Wang, Y.; Lu, L.; Peng, H.; Xu, J.; Wang, F.; Qi, R.; Xu, Z.; Zhang, 680
W. Multi-Doped Carbon Dots With Ratiometric Ph Sensing Properties 681
For Monitoring Enzyme Catalytic Reactions. *Chem. Commun.* **2016**, *52*, 682
9247–9250. 683
(33) Zhu, S.; Meng, Q.; Wang, L.; Zhang, J.; Song, Y.; Jin, H.; Zhang, 684
K.; Sun, H.; Wang, H.; Yang, B. Highly Photoluminescent Carbon Dots 685
For Multicolor Patterning, Sensors, And Bioimaging. *Angew. Chem., Int.* 686
Ed. **2013**, *52*, 3953–3957. 687
(34) Khanal, M.; Vausseil, T.; Barras, A.; Bande, O.; Turcheniuk, K.; 688
Benazza, M.; Zaitsev, V.; Teodorescu, C. M.; Boukherroub, R.; 689
Siriwardena, A.; Dubuisson, J.; Szunerits, S. Phenylboronic-Acid- 690
Modified Nanoparticles: Potential Antiviral Therapeutics. *ACS Appl.* 691
Mater. Interfaces **2013**, *5*, 12488–12498. 692